

**Multimode Brownian dynamics of a nanomechanical resonator in a viscous fluid**

H. Gress<sup>1</sup>,<sup>1</sup> J. Barbish<sup>2</sup>,<sup>2</sup> C. Yanik<sup>3,4</sup>,<sup>3,4</sup> I.I. Kaya<sup>3,4</sup>,<sup>3,4</sup> R.T. Erdogan<sup>5,6</sup>,<sup>5,6</sup> M.S. Hanay,<sup>5,6</sup>  
M. González,<sup>7</sup> O. Svitelskiy,<sup>8</sup> M.R. Paul<sup>2</sup>,<sup>2</sup> and K.L. Ekinci<sup>1,\*</sup>

<sup>1</sup>*Department of Mechanical Engineering, Division of Materials Science and Engineering, and the Photonics Center, Boston University, Boston, Massachusetts 02215, USA*

<sup>2</sup>*Department of Mechanical Engineering, Virginia Tech, Blacksburg, Virginia 24061, USA*

<sup>3</sup>*SUNUM, Nanotechnology Research and Application Center, Sabancı University, Istanbul 34956, Turkey*


<sup>4</sup>*Faculty of Engineering and Natural Sciences, Sabancı University, Istanbul 34956, Turkey*

<sup>5</sup>*Department of Mechanical Engineering, Bilkent University, Ankara 06800, Turkey*

<sup>6</sup>*National Nanotechnology Research Center (UNAM), Bilkent University, Ankara 06800, Turkey*

<sup>7</sup>*Aramco Americas, Aramco Research Center—Houston, Houston, Texas 77084, USA*

<sup>8</sup>*Department of Physics, Gordon College, Wenham, Massachusetts 01984, USA*

 (Received 4 April 2023; revised 25 September 2023; accepted 4 October 2023; published 24 October 2023)

Brownian motion imposes a hard limit on the overall precision of a nanomechanical measurement. Here, we present a combined experimental and theoretical study of the Brownian dynamics of a quintessential nanomechanical system, a doubly clamped nanomechanical beam resonator, in a viscous fluid. Our theoretical approach is based on the fluctuation-dissipation theorem of statistical mechanics: we determine the dissipation from fluid dynamics; we incorporate this dissipation into the proper elastic equation to obtain the equation of motion; and the fluctuation-dissipation theorem then directly provides an analytical expression for the position-dependent power spectral density (PSD) of the displacement fluctuations of the beam. We compare our theory to experiments on nanomechanical beams immersed in air and water and obtain excellent agreement. Within our experimental parameter range, the Brownian-force noise driving the nanomechanical beam has a colored PSD due to the “memory” of the fluid; the force noise remains mode independent and uncorrelated in space. These conclusions are not only of interest for nanomechanical sensing but also provide insight into the fluctuations of elastic systems at any length scale.

DOI: [10.1103/PhysRevApplied.20.044061](https://doi.org/10.1103/PhysRevApplied.20.044061)

**I. INTRODUCTION**

Brownian fluctuations of mechanical systems have been a topic of active research in physics since the 1920s [1,2]. Early electrometers [3] and galvanometers [4] that featured proof masses attached to linear springs displayed irregular movements around their equilibrium points despite all “precautions and shields” [5]. These early experiments eventually led to the realization that the observed fluctuations, namely, Brownian motion, were of a fundamental nature and limited the overall precision of mechanical measurements [5]. A century later, Brownian motion still remains centrally relevant to precision metrology and sensing based on mechanical systems—in particular, nanoelectromechanical systems (NEMS) [6] and AFM microcantilevers [7]. These state-of-the-art miniaturized mechanical systems are even more susceptible to Brownian noise

than their macroscopic counterparts, since they tend to be extremely compliant to forces.

The Brownian dynamics of a nanomechanical resonator can be formulated using elasticity theory and statistical mechanics. Elasticity theory provides a dissipationless equation of motion, such as the beam equation. Solving this equation under a harmonic ansatz and subject to boundary conditions maps the dynamics of the nanomechanical resonator onto that of a collection of eigenmodes, i.e., spring-mass systems, with discrete eigenfrequencies and mode shapes (eigenfunctions) [8,9]. In the simplest approximation of Brownian dynamics, each eigenmode is assumed to have a constant and spatially uniform dissipation, resulting in a Brownian-force noise that is delta-function correlated in both time and space. These assumptions result in a theoretical expression for the power spectral density (PSD) of the displacement fluctuations of the beam as a sum of the PSDs of the individual uncorrelated eigenmode fluctuations [8,10]. In the limit of small dissipation, multimode noise measurements on cantilevers [11],

\*[ekinci@bu.edu](mailto:ekinci@bu.edu)

microdisks [12], microtoroids [13], nanowires [14], and macroscopic elastic systems [15], all agree with this first-order approximation.

Most mechanical systems, however, *do* come with some “memory,” making the above-mentioned assumption of a temporally uncorrelated force noise inaccurate [8]. If the dissipation is spatially nonuniform, i.e., position dependent, the force noise between different eigenmodes becomes correlated [16], with the eigenmode expansion of the force noise becoming nontrivial. For elastic systems with spatially nonuniform dissipation, alternative approaches to calculate the noise PSD have been developed [16,17] and experimentally tested [18–20].

For a nanomechanical resonator immersed in a viscous fluid, memory comes from the flow-resonator interaction [21]. Here, the presence of the viscous fluid allows for a viable path to formulate the Brownian dynamics of the nanomechanical resonator consistently [22–24]: first, the dissipation of the resonator is found from fluid dynamics; then, the fluctuation-dissipation theorem is used for the calculation of the PSD of the resonator fluctuations. Since the fluidic dissipation is frequency dependent, the force-noise PSD is also “colored,” and the resonator fluctuations deviate substantially from the first-order approximation discussed above. In nearly all work so far, the dissipation in viscous fluids has been assumed to be mode independent and spatially uniform, resulting in a Brownian-force noise that is spatially uncorrelated. This assumption of spatial homogeneity again leads to formulas expressible as a sum in terms of the individual eigenmodes. There are notable papers, where the experimental noise data have been successfully fitted with colored PSDs. However, these experiments typically do not extend beyond the first mode of the elastic structure [25–28] and are thus not very insightful on the spatial nature of the force noise.

The topic of this paper is the Brownian dynamics of a nanomechanical resonator in a viscous fluid. In particular, we investigate how the Brownian force driving the nanomechanical resonator is correlated in time and space in a viscous fluid. To this end, we derive an expression for the PSD of the displacement fluctuations of an elastic nanomechanical beam under tension in a viscous fluid, assuming a frequency-dependent but spatially homogeneous viscous dissipation. This results in a PSD that is the sum of the PSDs of the uncorrelated fluctuations of individual eigenmodes. We validate this theory by experiments performed on nanomechanical beams under tension immersed in air and water. Using solely experimental parameters, we obtain excellent agreement between the experimental data and theory. This agreement, up to the 12th eigenmode in air and the seventh eigenmode in water, validates our overarching assumptions: the Brownian-force noise has a colored PSD due to the memory of the fluid but can be approximated to be uncorrelated in space.

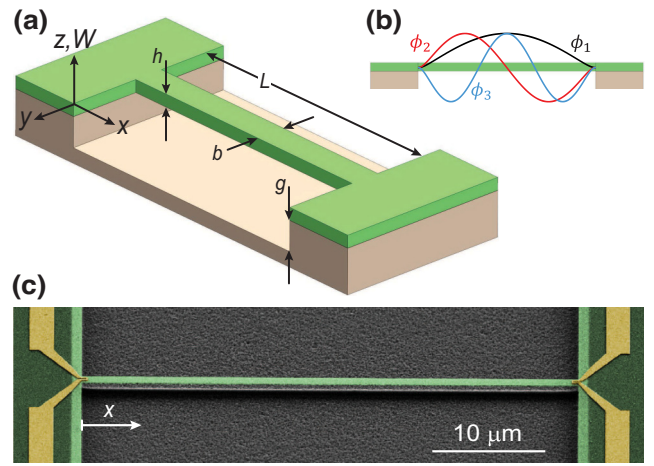


FIG. 1. (a) A doubly clamped beam with length  $L$ , width  $b$ , thickness  $h$ , and gap  $g$  between the beam and substrate. (b) An illustration of the first three eigenfunctions  $\phi_n(x)$ . (c) An SEM image of a doubly clamped silicon nitride beam under tension, with  $L \times b \times h = 50 \mu\text{m} \times 900 \text{ nm} \times 93 \text{ nm}$  and  $g = 2 \mu\text{m}$ . The silicon nitride layer is shown in green, with the suspended part in light green. The silicon substrate and the gold layer are gray and yellow, respectively.

## II. THEORY

We start with the equation of motion for a beam under tension driven by a deterministic external force in a viscous fluid. The respective linear dimensions of the beam are  $L \times b \times h$  along the  $x$ ,  $y$ , and  $z$  axes [Fig. 1(a)] and  $\mu = \rho_s b h$  is the mass per unit length, with  $\rho_s$  being the density. The flexural displacement of the beam,  $W(x, t)$ , along the  $z$  axis at position  $x$  and time  $t$  is given by

$$\begin{aligned} \frac{EI}{L^4} \frac{\partial^4 W(x, t)}{\partial x^4} - \frac{F_T}{L^2} \frac{\partial^2 W(x, t)}{\partial x^2} + \mu \frac{\partial^2 W(x, t)}{\partial t^2} \\ = F_f(x, t) + F_d(x, t). \end{aligned} \quad (1)$$

The  $x$  coordinate has been normalized by  $L$  such that  $0 \leq x \leq 1$ . In Eq. (1),  $E$  is the Young’s modulus,  $I$  is the area moment of inertia,  $F_f(x, t)$  is the force per unit length of the fluid acting on the beam,  $F_d(x, t)$  is the external drive force per unit length, and  $F_T$  is the tension [29]. The beam has fixed boundaries such that  $W(0, t) = W(1, t) = W'(0, t) = W'(1, t) = 0$ , where a prime indicates an  $x$  derivative.

It will be useful to proceed in the frequency domain [30], using the Fourier-transform pair

$$\hat{W}(x, \omega) = \int_{-\infty}^{\infty} W(x, t) e^{i\omega t} dt, \quad (2)$$

$$W(x, t) = \frac{1}{2\pi} \int_{-\infty}^{\infty} \hat{W}(x, \omega) e^{-i\omega t} d\omega, \quad (3)$$

where  $\omega$  is the angular frequency. This leads to the transformed differential equation

$$\frac{EI}{L^4} \frac{\partial^4 \hat{W}(x, \omega)}{\partial x^4} - \frac{F_T}{L^2} \frac{\partial^2 \hat{W}(x, \omega)}{\partial x^2} - \omega^2 \left[ \mu + \frac{\pi}{4} \rho_f b^2 \Gamma(\omega) \right] \hat{W}(x, \omega) = \hat{F}_d(x, \omega) \quad (4)$$

for the Fourier component  $\hat{W}(x, \omega)$  at  $\omega$ . In Eq. (4), we have described the force due to the fluid as

$$\hat{F}_f(x, \omega) = \frac{\pi}{4} \rho_f \omega^2 b^2 \Gamma(\omega) \hat{W}(x, \omega), \quad (5)$$

where  $\rho_f$  is the fluid density and  $\Gamma(\omega)$  is the complex hydrodynamic function for a blade, derived from Stokes' oscillating cylinder theory [31–33]. In Eq. (5),  $\Gamma(\omega)$  quantifies the mass loading and viscous damping of the fluid acting on the beams. To obtain  $\Gamma(\omega)$ , one starts with the complex hydrodynamic function for an infinitely long oscillating cylinder,

$$\Gamma_c(\text{Re}_\omega) = 1 + \frac{4iK_1(-i\sqrt{i\text{Re}_\omega})}{\sqrt{i\text{Re}_\omega}K_0(-i\sqrt{i\text{Re}_\omega})}, \quad (6)$$

where  $K_0$  and  $K_1$  are, respectively, the zeroth- and first-order modified Bessel functions of the second kind [34]. The argument of  $\Gamma_c$  is the frequency-dependent Reynolds number,  $\text{Re}_\omega = \rho_f \omega b^2 / 4\eta_f$ , where  $\eta_f$  is the dynamic viscosity of the fluid. To account for the rectangular cross section of the beams, one then applies a small frequency-dependent correction factor to  $\Gamma_c$  [33]. It can be deduced from Eq. (6) that the only parameters in  $\Gamma(\omega)$  are  $b$  and  $\eta_f$ , which are both constants. Thus,  $\Gamma(\omega)$  is assumed to be independent of position  $x$  as well as the mode shape of the beam.

We solve Eq. (4) using the eigenfunction expansion [33],

$$\hat{W}(x, \omega) = \sum_{n=1}^{\infty} f_n(\omega) \phi_n(x), \quad (7)$$

where  $n$  is the mode number,  $f_n(\omega)$  describes the frequency dependence, and the  $\phi_n(x)$  are the orthonormal eigenfunctions of the beam with tension [Fig. 1(b)]. Expressions for  $\phi_n(x)$  and the eigenfrequencies  $\omega_n/2\pi$  for a doubly clamped beam with tension are available [28,30,35,36]. We note that both  $\phi_n(x)$  and  $\omega_n/2\pi$  are found from the dissipationless equation of motion. The influence of the tension force on  $\phi_n(x)$  and  $\omega_n$  can be quantified in terms of the nondimensional tension parameter  $U$ , where  $F_T/(2EI/L^2)$ . The dynamics becomes, respectively, that of an Euler-Bernoulli beam and a string for  $U \rightarrow 0$  and  $U \gg 1$ .

Using the orthogonality of  $\phi_n(x)$ , the solution to Eq. (4) can be expressed as

$$\hat{W}(x, \omega) = \frac{L^4}{EI} \sum_{n=1}^{\infty} \frac{\int_0^1 \hat{F}_d(x', \omega) \phi_n(x') dx'}{\Omega_n^2 - B^4(\omega)} \phi_n(x). \quad (8)$$

$\Omega_n$  are the nondimensional eigenfrequencies, defined as

$$\Omega_n = \frac{\omega_n}{\alpha/L^2}, \quad (9)$$

where  $\alpha = (EI/\mu)^{1/2}$ . The complex function  $B(\omega)$  contains the dissipation and added mass and is given by

$$B^4(\omega) = \Omega_1^2 \left( \frac{\omega}{\omega_1} \right)^2 [1 + T_0 \Gamma(\omega)], \quad (10)$$

where  $\omega_1$  is the fundamental eigenfrequency of the beam in the absence of fluid, i.e., dissipation and added mass. The mass-loading parameter,  $T_0 = (\pi/4)(\rho_f b/\rho_s h)$ , is the ratio of the mass of a cylinder of fluid with diameter  $b$  to the mass of the beam.

In order to connect with the fluctuation-dissipation theorem, we next calculate the susceptibility,  $\hat{\chi}(x_0, t)$ , which we define as the time-dependent displacement of the beam measured at position  $x_0$  due to the application of a unit impulse of force at the same position  $x_0$ . Thus, we specify

$$F_d(x, t) = \frac{1}{L} \delta(x - x_0) \delta(t), \quad (11)$$

which becomes

$$\hat{F}_d(x, \omega) = \frac{1}{L} \delta(x - x_0) \quad (12)$$

in the frequency domain, with  $\delta$  being the Dirac delta function. Hence,  $\hat{\chi}(x_0, \omega) = \hat{W}(x_0, \omega)$  and we obtain

$$\hat{\chi}(x_0, \omega) = \frac{L^3}{EI} \sum_{n=1}^{\infty} \frac{\int_0^1 \delta(x' - x_0) \phi_n(x') dx'}{\Omega_n^2 - B^4(\omega)} \phi_n(x_0), \quad (13)$$

which can be expressed as

$$\hat{\chi}(x_0, \omega) = \frac{L^3}{EI} \sum_{n=1}^{\infty} \frac{\phi_n^2(x_0)}{\Omega_n^2 - B^4(\omega)}. \quad (14)$$

Using  $\omega_n/\omega_1 = \Omega_n/\Omega_1$ , defining  $\tilde{\omega}_n = \omega/\omega_n$ , and simplifying further yields

$$\hat{\chi}(x_0, \omega) = \sum_{n=1}^{\infty} \frac{1}{k_n(x_0)} \times \frac{1}{1 - \tilde{\omega}_n^2(1 + T_0 \Gamma'(\omega)) - i \tilde{\omega}_n^2 T_0 \Gamma''(\omega)}, \quad (15)$$

TABLE I. The eigenfrequencies  $\omega_n/2\pi$  are from fitting our air measurements to our model; the peak frequencies,  $\omega_n^{(v)}/2\pi$  and  $\omega_n^{(a)}/2\pi$ , are measured in vacuum and air, respectively. The effective stiffness  $k_n(x_n)$  is found at an antinode and the quality factors  $Q_n^{(a)}$  in air are found from Lorentzian fits. All frequency values are in megahertz. The modal peak for  $n = 12$  is barely resolvable in the PSD (Fig. 2).

Mode	$L = 30 \mu\text{m}$					$L = 40 \mu\text{m}$					$L = 50 \mu\text{m}$				
	$\frac{\omega_n}{2\pi}$	$\frac{\omega_n^{(v)}}{2\pi}$	$\frac{\omega_n^{(a)}}{2\pi}$	$k_n(x_n)$	$Q_n^{(a)}$	$\frac{\omega_n}{2\pi}$	$\frac{\omega_n^{(v)}}{2\pi}$	$\frac{\omega_n^{(a)}}{2\pi}$	$k_n(x_n)$	$Q_n^{(a)}$	$\frac{\omega_n}{2\pi}$	$\frac{\omega_n^{(v)}}{2\pi}$	$\frac{\omega_n^{(a)}}{2\pi}$	$k_n(x_n)$	$Q_n^{(a)}$
1	3.531	3.538	3.501	1.42	28	2.577	2.596	2.553	1.16	22	2.017	2.019	1.995	1.04	17
2	7.158	7.224	7.111	6.05	50	5.182	5.310	5.145	3.86	40	4.065	4.073	4.030	3.81	35
3	10.998	11.009	10.934	21.42	69	7.906	7.997	7.856	10.94	56	6.194	6.168	6.151	7.99	46
4	15.260	15.293	15.180	34.65	86	10.817	10.968	10.755	25.46	70	8.356	8.326	8.303	19.11	58
5	20.159	20.141	20.067	63.28	104	13.924	14.073	13.851	39.62	83	10.649	10.598	10.585	29.64	68
6	25.532	25.605	25.420	118.67	121	17.373	17.537	17.289	50.77	98	13.166	13.227	13.094	54.49	81
7	31.556	31.461	31.423	183.02	125	21.037	21.121	20.938	93.52	110	15.717	15.725	15.636	64.15	92
8	37.940	37.784	37.789	405.19	141	25.017	25.175	24.910	145.15	120	18.579	18.598	18.487	83.14	102
9	45.306	45.086	45.132	495.15	150	29.275	29.354	29.156	173.99	131	21.562	21.564	21.462	153.41	112
10	52.195	52.392	52.004	699.80	155	34.043	34.265	33.904	375.16	137	24.682	24.695	24.573	220.33	119
11	60.014	59.904	59.802	1077.36	167	38.970	38.879	38.817	375.16	144	28.112	27.988	27.991	220.33	128
12	...	68.342	68.293	...	...	44.291	44.234	44.120	564.47	153	31.678	31.565	31.548	349.46	136

where  $\Gamma'(\omega)$  and  $\Gamma''(\omega)$  are the real and imaginary parts of  $\Gamma(\omega)$ , respectively. The effective spring constant of mode  $n$ , when measured at  $x_0$ , is represented as  $k_n(x_0)$ ;  $k_n(x_0)$  can be consistently determined by ensuring that the kinetic energy of the spatially extended oscillating beam with mode shape  $\phi_n(x)$  equals that of a lumped system measured at  $x_0$ . This yields

$$k_n(x_0) = \frac{m\omega_n^2}{\phi_n^2(x_0)}, \quad (16)$$

where  $m = \mu L$  is the nominal mass of the beam.

The PSD of the Brownian fluctuations of the beam at axial position  $x_0$  can be directly expressed using the fluctuation-dissipation theorem [37,38] as

$$G_W(x_0, \omega) = \frac{4k_B T}{\omega} \hat{\chi}''(x_0, \omega), \quad (17)$$

where  $\hat{\chi}''(x_0, \omega)$  is the imaginary part of  $\hat{\chi}(x_0, \omega)$ ,  $k_B$  is the Boltzmann constant, and  $T$  is the temperature. The subscript  $W$  on  $G_W$  indicates that this is the spectral density of the fluctuations in the flexural displacement  $W(x, t)$  of the beam along the  $z$  axis.

Taking the imaginary part of Eq. (15) to find  $\hat{\chi}''(x_0, \omega)$  and inserting this into Eq. (17), we obtain the desired result as

$$G_W(x_0, \omega) = 4k_B T \sum_{n=1}^{\infty} \frac{1}{k_n(x_0)\omega_n} \times \frac{\tilde{\omega}_n T_0 \Gamma''(\omega)}{[1 - \tilde{\omega}_n^2(1 + T_0 \Gamma'(\omega))]^2 + [\tilde{\omega}_n^2 T_0 \Gamma''(\omega)]^2}. \quad (18)$$

This expression yields the total PSD for the displacement fluctuations of the beam at frequency  $\omega$  and position  $x_0$ . We emphasize that  $G_W(x_0, \omega)$  in Eq. (18) is obtained as a sum over individual eigenmodes. This is because  $\Gamma(\omega)$  is assumed to be spatially homogeneous and independent of mode number  $n$  [39].

### III. EXPERIMENTS

Our experiments are performed on silicon nitride doubly clamped beams of  $b = 900$  nm,  $h = 93$  nm, and three different lengths of  $L = 30, 40,$  and  $50 \mu\text{m}$ ; there is a gap of  $g = 2 \mu\text{m}$  between each beam and the substrate. Figure 1(c) shows a scanning electron microscope (SEM) image of a beam with  $L = 50 \mu\text{m}$ . All the beams are from the same fabrication batch. The beams are under tension, as inferred from their resonance frequencies in vacuum [29]. We determine  $\mu = \rho_s b h = 2.66 \times 10^{-10}$  kg/m, with the density measured as  $\rho_s = 2960$  kg/m<sup>3</sup> [29]. The beams also have U-shaped gold-nanoresistor patterns near their anchors for other experiments [28,29].

We measure the displacement fluctuations of the beams using a path-stabilized homodyne Michelson interferometer. The diffraction-limited He-Ne laser spot with a diameter of approximately  $650 \pm 10$  nm (full width at half maximum) is positioned on the beam using an XYZ precision stage. The typical powers incident on the beam and the photodetector are approximately  $600 \mu\text{W}$  and approximately  $1$  mW, respectively, with a shot-noise-limited displacement sensitivity of approximately  $5$  fm/ $\sqrt{\text{Hz}}$ . We calibrate the system against the wavelength of the laser [40] and operate at the point of optimal sensitivity. For each measurement taken at a given position  $x_0$  on a beam, a second measurement is taken with the same parameters near the anchor of the beam to determine the background noise

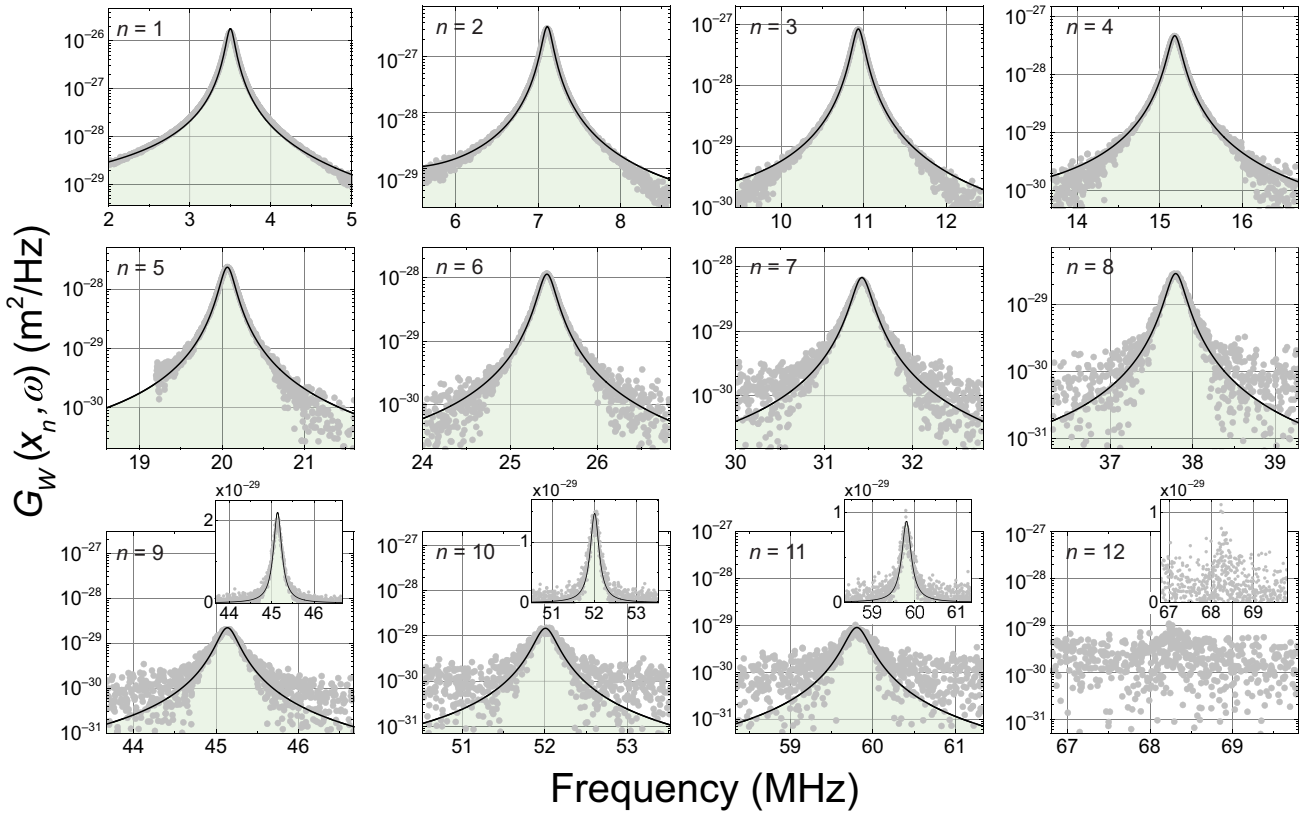


FIG. 2. The PSDs of the displacement fluctuations  $G_W(x_n, \omega)$  plotted using semilogarithmic axes for the first 12 modes of a beam with  $L = 30 \mu\text{m}$  in air. The measurement is performed at  $x = x_n$ , i.e., an antinode of mode  $n$ . The continuous lines are fits based on Eq. (18). The insets for  $n = 9, \dots, 12$  show  $G_W(x_n, \omega)$  using linear axes. Because the peak of the 12th mode is barely resolved, we do not determine values for  $\omega_{12}/2\pi$ ,  $k_{12}(x_{12})$ , and  $Q_{12}^{(a)}$ .

level in our measurements, e.g., due to the low-frequency laser noise or cable resonances. We assume that the beam fluctuations and the background noise are uncorrelated and subtract this background from the noise PSD measured on the beam [41]. This allows us to resolve the beam fluctuations down to approximately  $2 \text{ fm}/\sqrt{\text{Hz}}$ .

The finite size of the optical spot introduces errors into the measurements [42]. A significant source of error is the curvature of the beam, especially in higher modes. By computing the overlap of the Gaussian optical spot with the beam mode, we estimate this error to be less than 10% for the 12th mode of our 30- $\mu\text{m}$ -long beam, which has the largest curvature in all our experiments. In water measurements, it also becomes problematic to position the optical spot precisely at the desired locations on the beam. To find  $x_0 = 0.50$  (center) and  $x_0 = 0.25$  ( $L/4$ ) positions on the beam, we maximize the  $n = 1$  and  $n = 2$  peaks, respectively.

## IV. RESULTS

### A. Vacuum

We first measure the resonance frequencies of the eigenmodes of the beams in vacuum ( $p < 10^{-6}$  bar), as

listed in Table I. These peak frequencies in vacuum,  $\omega_n^{(v)}/2\pi$ , should be very close to the eigenfrequencies of the dissipationless beam,  $\omega_n/2\pi$ . We also extract quality factors in vacuum from Lorentzian fits and find that all  $Q_n^{(v)} \gtrsim 10^3$ .

### B. Air

Next, we examine the displacement fluctuations in air. We first identify the frequency at which our system transitions from viscous to molecular flow. For this system, the transition frequency  $\omega_c/2\pi$  can be found using  $\omega_c\tau + (\lambda/b) \approx 1$ , where  $\tau$  is the relaxation time and  $\lambda$  is the mean free path in the fluid [41,43]. In air,  $\tau \approx 1$  ns and  $\lambda \approx 68$  nm [41,43]. The relevant length scale,  $b = 900$  nm, is the same for all our devices. We thus find that  $\omega_c/2\pi \approx 100$  MHz in air. Therefore, our measurements are mostly within the viscous regime.

Figures 2–4, respectively, show the PSDs of the first 12 modes of beams with  $L = 30, 40,$  and  $50 \mu\text{m}$ . The low dissipation in air results in distinctly separated peaks in the PSDs. Each PSD is measured at an antinode ( $x = x_n$ ) of mode  $n$  as a function of frequency near the peak frequency,  $\omega_n^{(a)}/2\pi$ , in air. The relatively large modal quality

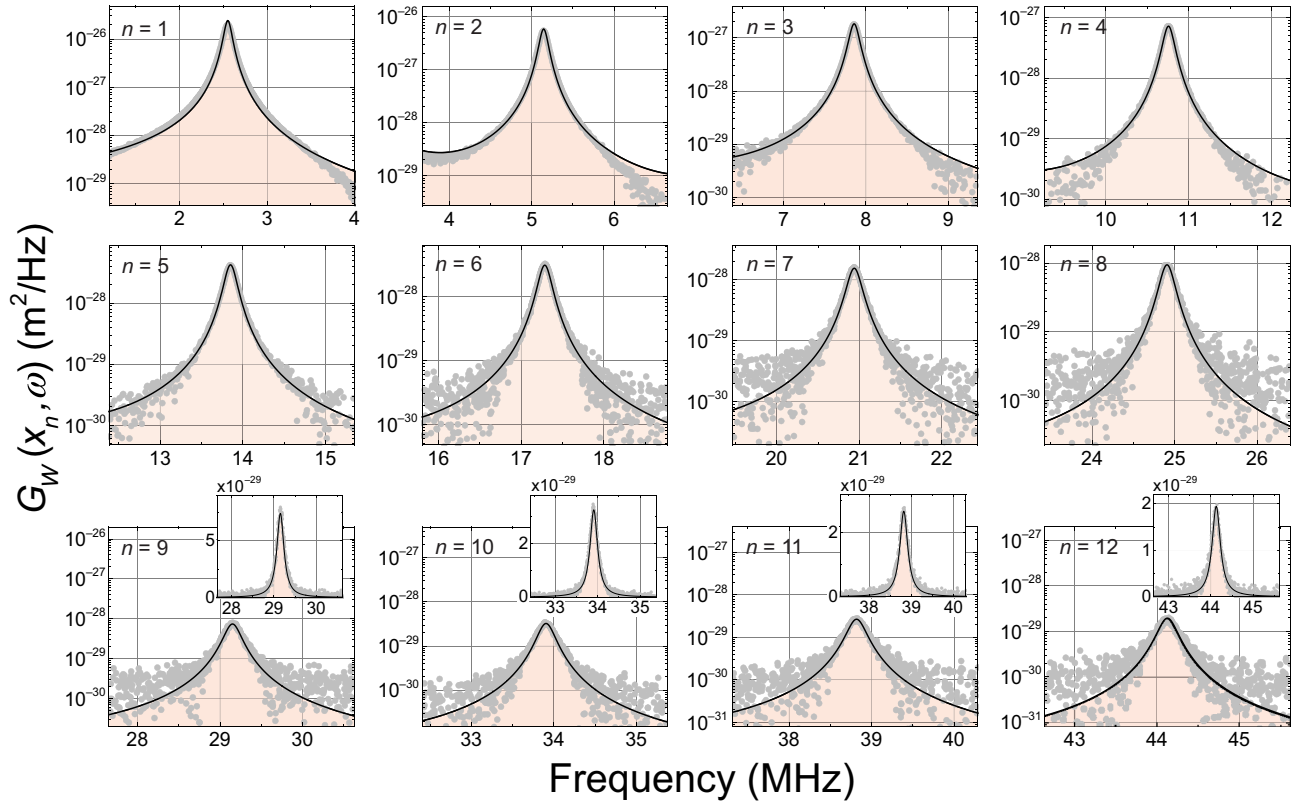


FIG. 3. The PSDs of the displacement fluctuations  $G_W(x_n, \omega)$  plotted using semilogarithmic axes for the first 12 modes of a beam with  $L = 40 \mu\text{m}$  in air. The measurement is performed at  $x = x_n$ , i.e., an antinode of mode  $n$ . The continuous lines are fits based on Eq. (18). The insets for  $n = 9, \dots, 12$  show  $G_W(x_n, \omega)$  using linear axes.

factors,  $17 \leq Q_n^{(a)} \leq 200$ , allow us to determine the eigenfrequencies  $\omega_n/2\pi$ , the effective spring constants  $k_n(x_n)$ , and the theoretical  $G_W(x_n, \omega)$  curves in a self-consistent manner. To this end, we first use the equipartition of energy to find  $k_n(x_n)$  from  $\frac{1}{2}k_n(x_n) \langle W_n^2(x_n) \rangle = \frac{1}{2}k_B T$ , where the mean-squared fluctuation amplitude,  $\langle W_n^2(x_n) \rangle$ , is the numerical integral of the experimental  $G_W(x_n, \omega)$  data over frequency. To find the theoretical  $G_W(x_n, \omega)$  curve, we calculate  $T_0$  and  $\Gamma(\omega)$  using the density and viscosity of air at room temperature. We then insert the experimental  $k_n(x_n)$  values along with  $T_0$  and  $\Gamma(\omega)$  into Eq. (18) and calculate  $G_W(x_n, \omega)$ , treating  $\omega_n$  as a fit parameter. The best fits are shown as continuous lines in Figs. 2–4.

We reemphasize that, except for  $\omega_n$ , the fits (continuous lines) in Figs. 2–4 are solely determined using known or measured quantities of the beam and the surrounding fluid. The values of  $\omega_n/2\pi$  found by fitting are typically slightly higher than  $\omega_n^{(a)}/2\pi$  (Table I). This is expected because the  $\omega_n/2\pi$  are the eigenfrequencies without any fluid loading. Our vacuum measurements support this observation (Table I): the vacuum frequencies  $\omega_n^{(v)}/2\pi$  are all slightly larger than  $\omega_n^{(a)}/2\pi$ . **There are very small discrepancies (typically <1.5%) between the eigenfrequencies determined by fitting, i.e.,  $\omega_n/2\pi$ , and those obtained from**

**vacuum measurements,  $\omega_n^{(v)}/2\pi$ . We attribute these small discrepancies to the fact that the eigenfrequencies of nanomechanical resonators are easily perturbed by external factors, e.g., the accumulation of adsorbates or changes in the temperature and humidity of the environment.** Since the resonance is very sharply peaked in air ( $Q_n^{(a)} > 10$ ) and in vacuum ( $Q_n^{(v)} \sim 10^3$ ), these perturbations result in small but noticeable frequency shifts from measurement to measurement.

### C. Eigenfrequencies and spring constants

We next compare the experimental values for  $\omega_n/2\pi$  and  $k_n(x_n)$  with the theoretical predictions of Euler-Bernoulli beam theory with tension [30]. We estimate the magnitude of the tension force  $F_T$  by comparing the eigenfrequencies obtained from experiments,  $\omega_n/2\pi$ , with those from theory,  $\omega_n^{(t)}/2\pi$ . To determine  $\omega_n^{(t)}/2\pi$ , we turn to the characteristic equation, which relates  $\omega_n^{(t)}/2\pi$  to the unknown tension [35] in terms of the nondimensional parameters  $\Omega_n$  and  $U$ . In our calculations, we use nominal beam dimensions as well as  $E$  and  $\rho_s$  values for SiN. Since the reported values for  $E$  have a large uncertainty,  $200 \text{ GPa} \lesssim E \lesssim 380 \text{ GPa}$  [44–46], we take the Young’s modulus as

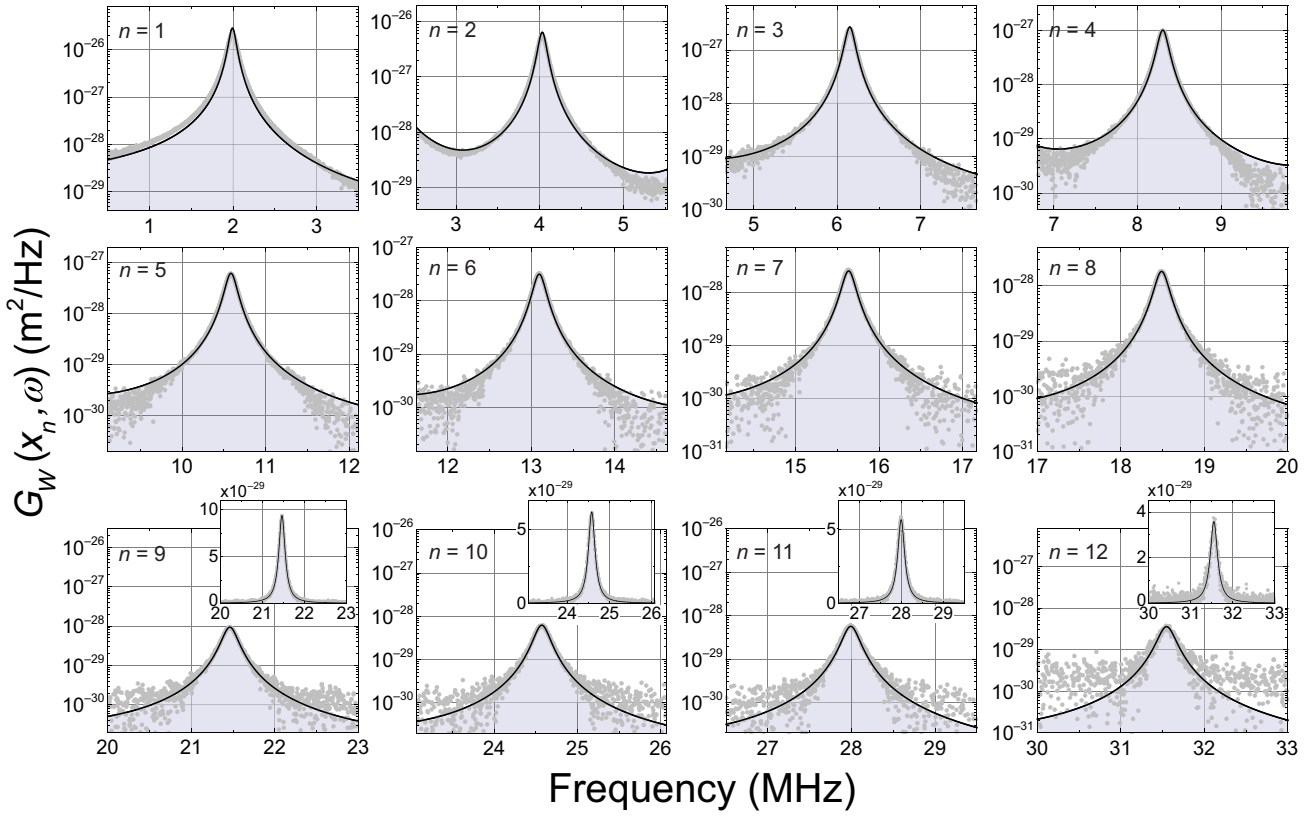


FIG. 4. The PSDs of the displacement fluctuations  $G_W(x_n, \omega)$  plotted using semilogarithmic axes for the first 12 modes of a beam with  $L = 50 \mu\text{m}$  in air. The measurement is performed at  $x = x_n$ , i.e., an antinode of mode  $n$ . The continuous lines are fits based on Eq. (18). The insets for  $n = 9, \dots, 12$  show  $G_W(x_n, \omega)$  using linear axes.

$E = 300 \text{ GPa}$ . The density has been measured as  $\rho_s = 2960 \pm 30 \text{ kg/m}^3$  [29]. For each beam, we sweep the value of  $F_T$ , solve for  $\omega_n^{(i)}/2\pi$  for each  $F_T$ , and then compute the error

$$\varepsilon = \sum_{n=1} \frac{|\omega_n - \omega_n^{(i)}|^2}{|\omega_n|^2} \quad (19)$$

between  $\omega_n$  and  $\omega_n^{(i)}$ , where  $n$  encompasses the first 12 modes. The minimum  $\varepsilon$  provides the experimental value of  $F_T$ . Because all of the beams are on the same chip, we average the values of  $F_T$  for each of our three beams. We thus find that  $F_T = 7.43 \mu\text{N}$ . In Fig. 5(a), we show experimental  $\omega_n/2\pi$  data (symbols) and theoretical predictions (continuous lines) using  $F_T = 7.43 \mu\text{N}$  on semilogarithmic axes for all three beams.

To find the theoretical  $k_n(x_n)$  at an antinode, we use Eq. (16). To this end, we calculate  $\phi_n(x)$  for each beam [30] using  $F_T$  and  $\omega_n/2\pi$ ; we use nominal  $m$ , measured  $\omega_n$ , and calculated  $\phi_n(x_n)$  to determine  $k_n(x_n)$ . We show the experimental and theoretical values for  $k_n(x_n)$  in Fig. 5(b). The experimental spring constants match predictions closely

over 2 orders of magnitude for  $n \lesssim 7$ . With our knowledge of  $\phi_n(x)$  and  $k_n(x_n)$ , we can determine  $k_n(x_0)$  for any position  $x_0$  along the beam.

The differences between the experimental and theoretical values of  $\omega_n$  and  $k_n(x_n)$  are most likely due to imperfections, such as the presence of the gold layer and the undercuts beneath the anchors. There is also an estimated 10% error in  $F_T$  due to the fact that we do not know the exact value of  $E$  [28]. Thus, it is more justifiable to use the  $\omega_n$  and  $k_n(x_n)$  values directly obtained from experiments rather than those calculated from elasticity theory.

#### D. Water

Our beams are then immersed in water, where we measure the PSDs of displacement fluctuations,  $G_W(x_0, \omega)$ , over the continuous frequency range of 50 kHz to 15 MHz at two positions on the beam,  $x_0 = 0.25$  and  $x_0 = 0.50$ . Figure 6 shows  $G_W(x_0, \omega)$  as a function of frequency at these two positions for all three beams. The first position,  $x_0 = 0.50$ , corresponds to an antinode of all odd modes and a node of all even modes [Figs. 6(a)–6(c)]; the second position,  $x_0 = 0.25$ , is close to the antinode of the second mode [Figs. 6(d)–6(f)]. Low quality factors

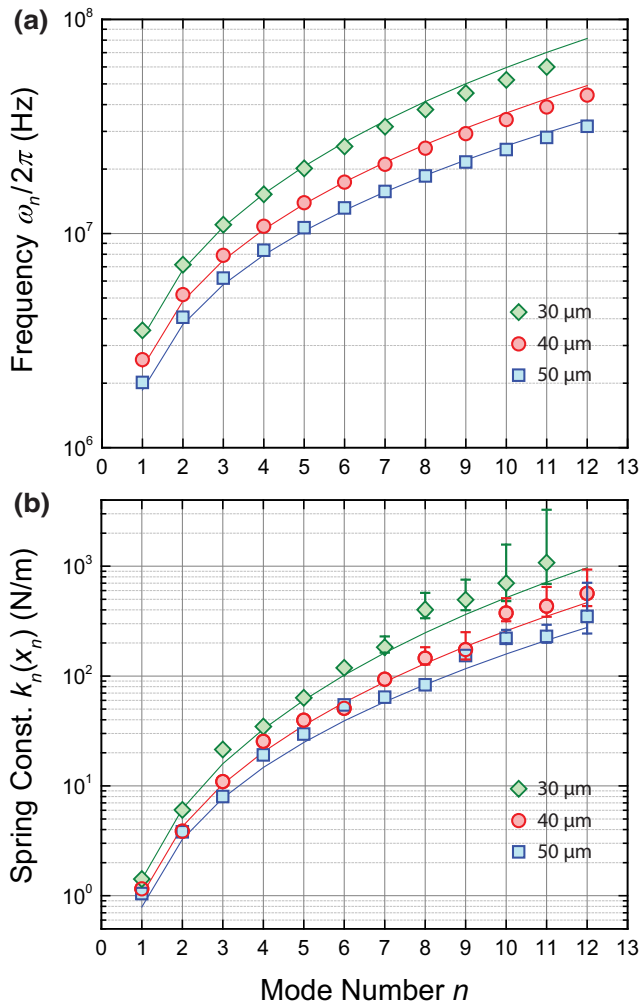


FIG. 5. The (a) eigenfrequencies  $\omega_n/2\pi$  and (b) effective spring constants  $k_n(x_n)$  for beams with  $L = 30 \mu\text{m}$ ,  $L = 40 \mu\text{m}$ , and  $L = 50 \mu\text{m}$ . Experimental values and theoretical predictions are shown by symbols and continuous lines, respectively. Typical error bars for  $k_n(x_n)$  are smaller than the symbols, unless shown explicitly.

( $Q \gtrsim 1$ ) in water result in broad and overlapping peaks; the peak frequencies are significantly lower than those in air.

Next, we compare our measurements in water to our theoretical expression for  $G_W(x_0, \omega)$ . The continuous curves in Fig. 6 show predictions based on Eq. (18). Here, we use the  $\omega_n$  values found above and determine  $k_n(x_0)$  from  $k_n(x_n)$  after correcting for the position dependence via Eq. (16). We then compute  $T_0$  and  $\Gamma(\omega)$  using the density and viscosity of water and combine all factors in Eq. (18) to generate the curves. The dotted curves show the PSDs of individual modes; the continuous curve is the sum of the first 12 modes. A strong agreement between experiment and theory is evident for  $n \lesssim 7$ ; for  $n \gtrsim 7$ , the beam fluctuations remain below our resolution limit. The theory

predicts the peak frequencies and the noise power levels accurately.

The positioning error mentioned in the third paragraph in Sec. III affects both  $k_n(x_0)$  and the measured  $G_W(x_0, \omega)$ . This error becomes more pronounced at higher frequencies. In principle, the theory curves can be further improved by treating the measurement position as a fit parameter.

## V. DISCUSSION AND CONCLUSIONS

Equation (18) describes the Brownian dynamics of a nanomechanical beam in a viscous fluid and indicates that, at a given frequency, the total noise is found by adding the noise PSDs in different eigenmodes. The underlying assumption is that the Brownian-force noise is delta-function correlated in space [33,47]. The form of Eq. (18), i.e., the summation over uncorrelated eigenmodes, should remain unchanged for any mechanical system as long as the dissipation is uniform in space. For our system, the dissipation in Eq. (5) from the cylinder model is indeed spatially homogeneous. The remarkable agreement between experiment and theory in Fig. 6 for the first seven modes suggests that the cylinder model remains accurate—to within our experimental resolution. In other words, the frequency dependence and the spatial homogeneity of the dissipation in the model are both validated by our experiments.

Hydrodynamic fluctuations in a simple fluid are typically assumed to be delta-function correlated in space [48]. However, the situation is different for the nanomechanical beam immersed in a fluid: the flow around the structure and the fluid-structure interactions are expected to result in spatial correlations in the force noise, eventually leading to observable deviations from Eq. (18) for higher modes. This expectation is consistent with the fact that the viscous dissipation of the oscillating-cylinder model is not accurate for higher modes. As the flow in the axial direction becomes more appreciable with increasing mode number, the dissipation becomes mode dependent and nonuniform [39,49]. However, the agreement between predictions and experiments suggests that the axial flow is negligible in our parameter space. The smallest length scale probed in our beams is comparable to the smallest resolved modal wavelength of approximately  $9 \mu\text{m}$ .

$G_W(x_0, \omega)$  should also be affected by the presence of the nearby substrate due to the squeeze flow between the beam and the substrate. In our theory, we have neglected the presence of the substrate. This can be corrected using numerical simulations [49]: we estimate a decrease in  $\Gamma'(\omega/2\pi = 0.1 \text{ MHz})$  by approximately 30% and an increase in  $\Gamma''(\omega/2\pi = 0.1 \text{ MHz})$  by approximately 30%, which leads to an increase in  $G_W(\omega/2\pi = 0.1 \text{ MHz}, x_0)$  of  $\lesssim 30\%$  depending on the length  $L$  of the beam. This



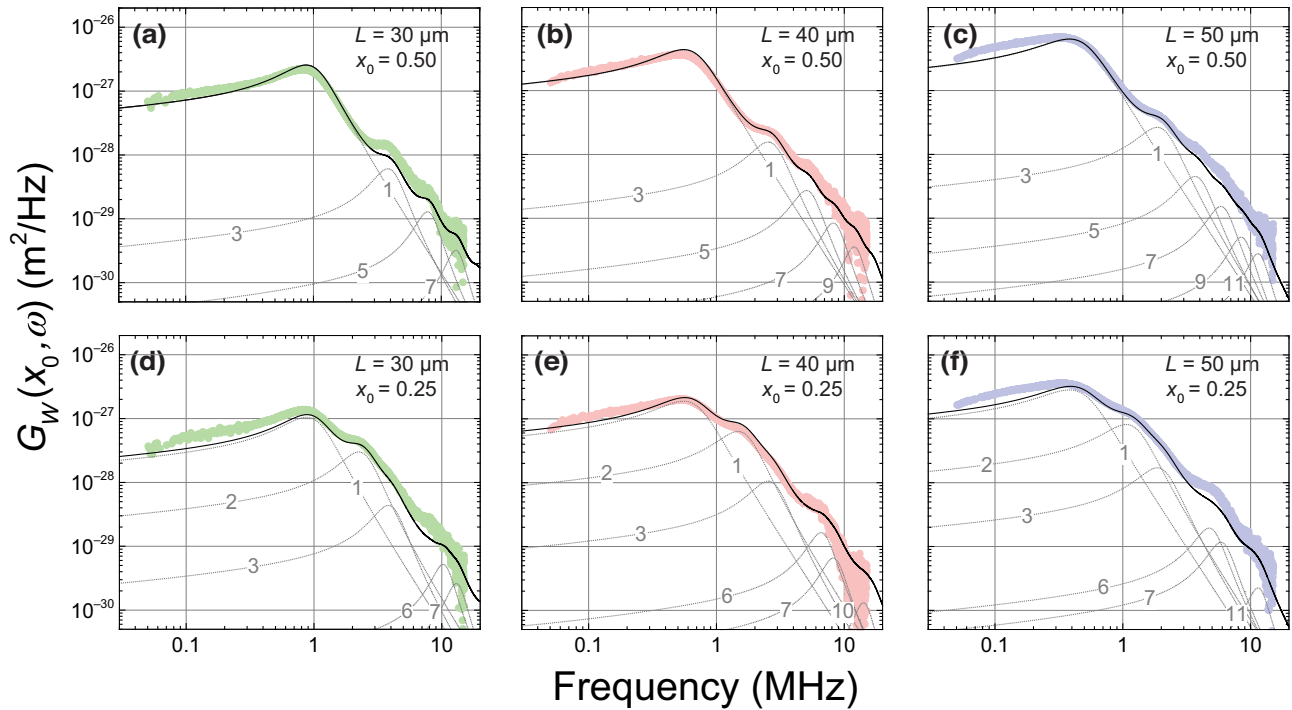


FIG. 6. The PSDs of the displacement fluctuations  $G_W(x_0, \omega)$  at (a)–(c)  $x_0 = 0.50$  and (d)–(f)  $x_0 = 0.25$  for three beams with different lengths in water. The continuous lines are predictions of Eq. (18) based on experimental parameters. The dotted lines show the contributions of individual modes  $n$  to  $G_W(x_0, \omega)$ . Modes not shown do not contribute significantly at the particular  $x_0$ .

additional damping should further broaden the fundamental mode and induce an additional red shift of the peak [25,50], which we observe in measurements. At higher frequencies, as the thickness of the viscous boundary layer  $\delta$  becomes  $\delta/g \ll 1$ , this effect disappears [27,51].

To experimentally observe the noise-correlation effects due to fluid-structure interaction, it would be necessary to resolve the fluctuations in higher modes. To this end, one should first determine the viscous dissipation from fluid dynamics and assess the regime where the dissipation becomes nonhomogenous, e.g., due to axial flows. Unfortunately, analytical solutions cannot be found for most experimental geometries, making numerical simulations necessary. Once the flow regimes around the structure are determined, one could design and fabricate structures with softer spring constants  $k_n$  such that the Brownian motions in higher modes can be resolved.

Nonlinearities in the elastic potential can modify the Brownian dynamics of the nanomechanical beam [52,53]. Achieving the nonlinear limit for thermal fluctuations of a mode requires a very high modal  $Q_n$  and a very soft modal spring [53]. We estimate that the very low  $Q_n$  in fluids along with the large  $k_n$  of the beams makes nonlinear effects negligible in our experiments. As an order-of-magnitude comparison, the fundamental mode of our 50- $\mu\text{m}$ -long beam displays nonlinear behavior at amplitudes  $\gtrsim 20$  nm [54], while its thermal amplitude remains around 60 pm in air. The emergence of nonlinear behavior

in higher modes of elastic structures and Brownian motion in a nonlinear potential are both interesting questions requiring further study.

## ACKNOWLEDGMENTS

We acknowledge support from the U.S. National Science Foundation (NSF) through Grants No. CMMI-2001559, No. CMMI-1934271, No. CMMI-1934370, and No. CMMI-2001403.

- 
- [1] G. E. Uhlenbeck and L. S. Ornstein, On the theory of the Brownian motion, *Phys. Rev.* **36**, 823 (1930).
  - [2] E. Kappler, Versuche zur Messung der Avogadro-Loschmidtschen Zahl aus der Brownschen Bewegung einer Drehwaage, *Ann. Phys. (Leipzig)* **403**, 233 (1931).
  - [3] A. Parson, A highly sensitive electrometer, *Phys. Rev.* **6**, 390 (1915).
  - [4] W. Moll and H. Burger, LXV. The sensitivity of a galvanometer and its amplification, *Lond. Edinb. Dublin Philos. Mag. J. Sci.* **50**, 626 (1925).
  - [5] R. B. Barnes and S. Silverman, Brownian motion as a natural limit to all measuring processes, *Rev. Mod. Phys.* **6**, 162 (1934).
  - [6] A. Bachtold, J. Moser, and M. I. Dykman, Mesoscopic physics of nanomechanical systems, *Rev. Mod. Phys.* **94**, 045005 (2022).

- [7] H.-J. Butt and M. Jaschke, Calculation of thermal noise in atomic force microscopy, *Nanotechnology* **6**, 1 (1995).
- [8] P. R. Saulson, Thermal noise in mechanical experiments, *Phys. Rev. D* **42**, 2437 (1990).
- [9] A. N. Cleland, *Foundations of Nanomechanics* (Springer-Verlag, Berlin, 2013).
- [10] A. N. Cleland and M. L. Roukes, Noise processes in nanomechanical resonators, *J. Appl. Phys.* **92**, 2758 (2002).
- [11] P. Paolino, B. Tiribilli, and L. Bellon, Direct measurement of spatial modes of a microcantilever from thermal noise, *J. Appl. Phys.* **106**, 094313 (2009).
- [12] Z. Wang, J. Lee, and P. X.-L. Feng, Spatial mapping of multimode Brownian motions in high-frequency silicon carbide microdisk resonators, *Nat. Commun.* **5**, 1 (2014).
- [13] T. G. McRae, K. H. Lee, G. I. Harris, J. Knittel, and W. P. Bowen, Cavity optoelectromechanical system combining strong electrical actuation with ultrasensitive transduction, *Phys. Rev. A* **82**, 023825 (2010).
- [14] A. Gluppe, P. Verlot, E. Dupont-Ferrier, A. Siria, P. Poncharal, G. Bachelier, P. Vincent, and O. Arcizet, Bidimensional nano-optomechanics and topological backaction in a non-conservative radiation force field, *Nat. Nanotechnol.* **9**, 920 (2014).
- [15] O. Arcizet, P.-F. Cohadon, T. Briant, M. Pinard, A. Heidmann, J.-M. Mackowski, C. Michel, L. Pinard, O. Français, and L. Rousseau, High-sensitivity optical monitoring of a micromechanical resonator with a quantum-limited optomechanical sensor, *Phys. Rev. Lett.* **97**, 133601 (2006).
- [16] Y. Levin, Internal thermal noise in the LIGO test masses: A direct approach, *Phys. Rev. D* **57**, 659 (1998).
- [17] Y. T. Liu and K. S. Thorne, Thermoelastic noise and homogeneous thermal noise in finite sized gravitational-wave test masses, *Phys. Rev. D* **62**, 122002 (2000).
- [18] K. Yamamoto, S. Otsuka, M. Ando, K. Kawabe, and K. Tsubono, Experimental study of thermal noise caused by an inhomogeneously distributed loss, *Phys. Lett. A* **280**, 289 (2001).
- [19] K. Yamamoto, S. Otsuka, M. Ando, K. Kawabe, and K. Tsubono, Study of the thermal noise caused by inhomogeneously distributed loss, *Class. Quantum Gravity* **19**, 1689 (2002).
- [20] C. Schwarz, B. Pigeau, L. M. De Lépinay, A. G. Kuhn, D. Kalita, N. Bendiab, L. Marty, V. Bouchiat, and O. Arcizet, Deviation from the normal mode expansion in a coupled graphene-nanomechanical system, *Phys. Rev. Appl.* **6**, 064021 (2016).
- [21] T. Franosch, M. Grimm, M. Belushkin, F. M. Mor, G. Foffi, L. Forró, and S. Jeney, Resonances arising from hydrodynamic memory in Brownian motion, *Nature* **478**, 85 (2011).
- [22] M. R. Paul and M. C. Cross, Stochastic dynamics of nanoscale mechanical oscillators immersed in a viscous fluid, *Phys. Rev. Lett.* **92**, 235501 (2004).
- [23] M. R. Paul, M. T. Clark, and M. C. Cross, The stochastic dynamics of micron and nanoscale elastic cantilevers in fluid: Fluctuations from dissipation, *Nanotechnology* **17**, 4502 (2006).
- [24] M. T. Clark, J. E. Sader, J. P. Cleveland, and M. R. Paul, Spectral properties of microcantilevers in viscous fluid, *Phys. Rev. E* **81**, 046306 (2010).
- [25] R. J. Clarke, O. E. Jensen, J. Billingham, A. P. Pearson, and P. M. Williams, Stochastic elasto-hydrodynamics of a microcantilever oscillating near a wall, *Phys. Rev. Lett.* **96**, 050801 (2006).
- [26] L. Bellon, Thermal noise of microcantilevers in viscous fluids, *J. Appl. Phys.* **104**, 104906 (2008).
- [27] E. Pierro, F. Bottiglione, and G. Carbone, Thermal fluctuations and dynamic modeling of a dAFM cantilever, *Adv. Theory Simul.* **2**, 1900004 (2019).
- [28] A. B. Ari, M. S. Hanay, M. R. Paul, and K. L. Ekinci, Nanomechanical measurement of the Brownian force noise in a viscous liquid, *Nano Lett.* **21**, 375 (2020).
- [29] C. Ti, A. B. Ari, M. C. Karakan, C. Yanik, I. I. Kaya, M. S. Hanay, O. Svitelskiy, M. González, H. Seren, and K. L. Ekinci, Frequency-dependent piezoresistive effect in top-down fabricated gold nanoresistors, *Nano Lett.* **21**, 6533 (2021).
- [30] J. Barbish, C. Ti, K. L. Ekinci, and M. R. Paul, The dynamics of an externally driven nanoscale beam that is under high tension and immersed in a viscous fluid, *J. Appl. Phys.* **132**, 034501 (2022).
- [31] H. Schlichting, Berechnung ebener periodischer Grenzschichtströmungen, *Phys. Z.* **33**, 327 (1932).
- [32] T. Retsina, S. Richardson, and W. Wakeham, The theory of a vibrating-rod viscometer, *Appl. Sci. Res.* **43**, 325 (1987).
- [33] J. E. Sader, Frequency response of cantilever beams immersed in viscous fluids with applications to the atomic force microscope, *J. Appl. Phys.* **84**, 64 (1998).
- [34] L. Rosenhead, *Laminar Boundary Layers* (Clarendon, Oxford, 1963).
- [35] A. Bokaian, Natural frequencies of beams under tensile axial loads, *J. Sound Vib.* **142**, 481 (1990).
- [36] I. Stachiv, Impact of surface and residual stresses and electro-/magnetostatic axial loading on the suspended nanomechanical based mass sensors: A theoretical study, *J. Appl. Phys.* **115**, 214310 (2014).
- [37] H. B. Callen and T. A. Welton, Irreversibility and generalized noise, *Phys. Rev.* **83**, 34 (1951).
- [38] H. B. Callen and R. F. Greene, On a theorem of irreversible thermodynamics, *Phys. Rev.* **86**, 702 (1952).
- [39] C. Van Eysden and J. E. Sader, Frequency response of cantilever beams immersed in viscous fluids with applications to the atomic force microscope: Arbitrary mode number, *J. Appl. Phys.* **101**, 044908 (2007).
- [40] J. W. Wagner, Optical detection of ultrasound, *Phys. Acoust.* **19**, 201 (1990).
- [41] V. Kara, Y.-I. Sohn, H. Atikian, V. Yakhot, M. Loncar, and K. L. Ekinci, Nanofluidics of single-crystal diamond nanomechanical resonators, *Nano Lett.* **15**, 8070 (2015).
- [42] T. Kouh, D. Karabacak, D. Kim, and K. Ekinci, Diffraction effects in optical interferometric displacement detection in nanoelectromechanical systems, *Appl. Phys. Lett.* **86**, 013106 (2005).
- [43] V. Kara, V. Yakhot, and K. L. Ekinci, Generalized Knudsen number for unsteady fluid flow, *Phys. Rev. Lett.* **118**, 074505 (2017).
- [44] Y.-C. Tai and R. Muller, in *Proceedings on Micro Electro Mechanical Systems, An Investigation of Micro Structures, Sensors, Actuators, Machines and Robots* (IEEE, Napa Valley, 1990), p. 147.

- [45] T.-Y. Zhang, Y.-J. Su, C.-F. Qian, M.-H. Zhao, and L.-Q. Chen, Microbridge testing of silicon nitride thin films deposited on silicon wafers, *Acta Mater.* **48**, 2843 (2000).
- [46] J. L. Kuhn, R. K. Fetting, S. H. Moseley Jr, A. S. Kuttyrev, and J. Orloff, in *MEMS Reliability for Critical Applications*, Vol. 4180 (SPIE, Santa Clara, 2000), p. 40.
- [47] D. E. Newland, *An Introduction to Random Vibrations, Spectral & Wavelet Analysis* (Dover Publications, New York, 2012).
- [48] L. D. Landau, E. Lifshitz, and L. Pitaevskii, *Course of Theoretical Physics: Statistical Physics, Part 2* (Pergamon, Oxford, 1980).
- [49] A. T. Liem, A. B. Ari, C. Ti, M. J. Cops, J. G. McDaniel, and K. L. Ekinci, Nanoflows induced by MEMS and NEMS: Limits of two-dimensional models, *Phys. Rev. Fluids* **6**, 024201 (2021).
- [50] C. P. Green and J. E. Sader, Frequency response of cantilever beams immersed in viscous fluids near a solid surface with applications to the atomic force microscope, *J. Appl. Phys.* **98**, 114913 (2005).
- [51] R. J. Clarke, S. M. Cox, P. Williams, and O. Jensen, The drag on a microcantilever oscillating near a wall, *J. Fluid Mech.* **545**, 397 (2005).
- [52] M. Dykman and M. Krivoglaz, Classical theory of non-linear oscillators interacting with a medium, *Phys. Status Solidi (B)* **48**, 497 (1971).
- [53] J. Gieseler, L. Novotny, and R. Quidant, Thermal nonlinearities in a nanomechanical oscillator, *Nat. Phys.* **9**, 806 (2013).
- [54] H. Postma, I. Kozinsky, A. Husain, and M. Roukes, Dynamic range of nanotube- and nanowire-based electromechanical systems, *Appl. Phys. Lett.* **86**, 223105 (2005).